CHAPTER IV

RESULTS AND DISCUSSION

4.1 XRF Analysis

X-ray fluorescence (XRF) spectroscopy was used to characterize the composition of the white clay feedstock and the synthesized zeolite A. The analysis aimed to evaluate the extent of clay transformation during synthesis and to confirm the formation of a zeolitic structure by monitoring compositional changes, particularly variations in the Si/Al ratio and sodium content. Table 4.1 presents the comparative XRF results for the different white clay samples and the resulting zeolite products. The raw clay was predominantly composed of silica (SiO_2) and alumina (Al_2O_3), with minor amounts of iron oxide (Fe_2O_3) potassium oxide (K_2O), calcium oxide (CaO), and magnesium oxide (MgO).

The raw ball clay was analyzed for its elemental composition using X-ray fluorescence spectroscopy (XRF). The results of the analysis are shown in Table 4.1. It was found that the raw ball clay contained 55.946% w/w SiO_2 and 36.085% w/w Al_2O_3, with a molar ratio of 1.32. The Si/Al molar ratio of 1.32 was used to synthesize the Na-A zeolite without any adjustment. In addition, the raw ball clay also contained small amounts of elements such as iron oxide (Fe_2O_3), potassium oxide (K_2O), calcium oxide (CaO), titanium dioxide (TiO_2), and manganese dioxide (MnO_2). Moreover, the SiO_2/Al_2O_3 molar ratio closely matches the theoretical ratio for zeolite A synthesis, as confirmed by the calculation below Table 4.1, indicating a successful structural transformation. These results demonstrate the effectiveness of using white clay as a raw material for synthesizing zeolite A and achieving the elemental composition through the applied synthesis process.

Following the synthesis, a notable increase in the Na_2O content was detected in the zeolite A sample, which indicates that sodium was effectively integrated into the crystal structure during the hydrothermal treatment. This substantial rise in Na_2O correlates strongly with both the mechanism of formation and the stabilization of the zeolite framework. Sodium ions (Na^+), sourced from Na_2O, are crucial as structure-directing and charge-compensating agents, especially in low-silica zeolites like zeolite A (LTA-type). Their presence aids in the formation of a well-organized aluminosilicate framework by balancing the negative charges caused by the isomorphic substitution of Si^{4+} by Al^{3+} in the tetrahedral structure. An increase in Na_2O concentration also boosts the alkalinity of the reaction medium, which is vital for enhancing the dissolution of silica and alumina sources. This improved solubility speeds up the nucleation and crystallization processes of zeolite structures through a dissolution–reprecipitation mechanism. Furthermore, the Na_2O levels have a direct effect on phase selectivity during hydrothermal synthesis. Lower sodium levels typically result in amorphous or poorly crystalline phases, while higher Na_2O concentrations promote the formation of sodium-rich crystalline zeolite phases like zeolite A. This phenomenon is linked to the role of Na^+ in stabilizing intermediate aluminosilicate species and facilitating the assembly of the desired microporous framework.

Table 4.1 The chemical XRF composition of raw materials and zeolite A

Element	**Ball clay (wt%)**	**Lampang white clay (wt%)**	**Ranong white clay (wt%)**	**Na-A Zeolite (wt%)**
SiO_2	55.946	64.478	73.519	42.856
Al_2O_3	36.085	24.763	13.223	36.619
Fe_2O_3	1.141	1.268	2.209	1.207

Table 4.1 The chemical XRF composition of raw materials and zeolite A (Continued)

Element	Ball clay (wt%)	Lampang white clay (wt%)	Ranong white clay (wt%)	Na-A Zeolite (wt%)
K_2O	0.377	3.973	3.285	2.123
TiO_2	0.346	0.046	0.089	0.030
CaO	0.096	0.212	0.104	0.124
MnO_2	0.009	0.246	0.071	0.020
Na_2O	3.178	4.196	5.232	16.456
MgO	2.822	0.818	2.268	0.565

1. Si/Al calculation of Ball Clay

$$SiO_2 = \frac{55.946 \times 258.18}{100 \times 60.08} = 2.40 \text{ mol}$$

$$Al_2O_3 = \frac{36.085 \times 258.18}{100 \times 101.96} = 0.91 \text{ mol}$$

$$Si/Al = \frac{2.40}{0.91 \times 2} = 1.32$$

2. Si/Al calculation of Lampang white clay

$$SiO_2 = \frac{64.478 \times 258.18}{100 \times 60.08} = 2.77 \text{ mol}$$

$$Al_2O_3 = \frac{24.763 \times 258.18}{100 \times 101.96} = 0.63 \text{ mol}$$

$$\text{Si/Al} = \frac{2.77}{0.63 \times 2} = 2.20$$

3. Si/Al calculation of Ranong white clay

$$SiO_2 = \frac{73.519 \times 258.18}{100 \times 60.08} = 3.16 \text{ mol}$$

$$Al_2O_3 = \frac{13.223 \times 258.18}{100 \times 101.96} = 0.33 \text{ mol}$$

$$\text{Si/Al} = \frac{3.16}{0.33 \times 2} = 4.79$$

4. Si/Al calculation of Na-A Zeolite

$$SiO_2 = \frac{42.856 \times 1807.26}{100 \times 60.08} = 12.89 \text{ mol}$$

$$Al_2O_3 = \frac{36.619 \times 1807.26}{100 \times 101.96} = 6.49 \text{ mol}$$

$$\text{Si/Al} = \frac{12.89}{6.49 \times 2} = 0.99$$

Notation:

SiO_2 = 60.08 g/mol

Al_2O_3 = 101.96 g/mol

Ball clay, Ranong white clay, Lampang white clay = 258.18 g/mol

Zeolite A = 1807.26 g/mol

SiO_2 (wt%) of ball clay = 55.946 g/mol

Al_2O_3 (wt%) of ball clay = 36.085 g/mol

SiO_2 (wt%) of Lampang white clay = 64.478 g/mol

Al_2O_3 (wt%) of Lampang white clay = 24.763 g/mol

SiO_2 (wt%) of Ranong white clay = 73.519 g/mol

Al_2O_3 (wt%) of Ranong white clay = 13.223 g/mol

SiO_2 (wt%) of Na-A zeolite = 42.856 g/mol

Al_2O_3 (wt%) of Na-A zeolite = 36.619 g/mol

In calculating the molar ratio of silicon to aluminum (Si/Al) within the zeolite framework (or the precursor mix used for synthesis), meticulous consideration must be given to the atomic stoichiometry of the corresponding oxide sources. Specifically, silicon dioxide (SiO_2) contributes one atom of silicon (Si) per formula unit, while aluminum oxide (Al_2O_3) contributes two atoms of aluminum (Al) per formula unit. Therefore, if the starting molar ratio is defined based on the quantities of SiO_2 and Al_2O_3, the true atomic ratio of Si/Al requires a correction factor. This correction involves multiplying the number of moles of Al_2O_3 by a factor of 2 to accurately reflect the actual number of aluminum atoms present in the mixture.

4.2 Thermal Analysis

The thermal behavior of the ball clay sample was investigated by thermogravimetric analysis (TGA) and differential thermal analysis (DTA), as shown in Figure 4.1 The TGA curve (blue line) and DTA curve (red line) reveal the mass changes and corresponding thermal behavior occurring during heating from 30 °C to 1000 °C in an oxygen atmosphere at 10 °C/min.

In the first stage, approximately 1–2% weight loss occurred at the heat below 100°C, accompanied by a small endothermic effect in the DTA curve. This change

corresponds to the evaporation of physically adsorbed and interlayer water molecules, indicating the removal of surface moisture and loosely bound water from the ball clay structure.

The second stage, occurring in the temperature range of 280–560 °C, exhibits a major endothermic peak with a maximum at 510 °C corresponding to the dihydroxylation of kaolinite, the principal mineral phase in ball clay. During this process, the structural hydroxyl groups within the kaolinite structure are removed.

This transformation leads to the formation of metakaolin, an amorphous and highly reactive aluminosilicate phase. The endothermic peak observed at 510 °C confirms the energy absorption associated with the breakdown of the kaolinite crystal structure. Beyond 680 °C, the TGA curve gradually levels off, indicating that the dehydroxylation process is nearly complete. No significant mass loss is detected above this temperature. The material thus transitions into a thermally stable metastable phase, suitable as a precursor for zeolite synthesis. The formation of metakaolin within the 510–680 °C temperature window is of particular importance for zeolite synthesis because it increases the reactivity of silicon and aluminum species during hydrothermal treatment. This ensures more efficient dissolution and reassembly of the aluminosilicate network into the crystalline framework of zeolite A. Therefore, based on the thermal analysis results, the optimal calcination temperature range for preparing reactive ball clay lies between 510 °C and 680°C, ensuring complete dehydroxylation and maximizing the potential for zeolite A formation.

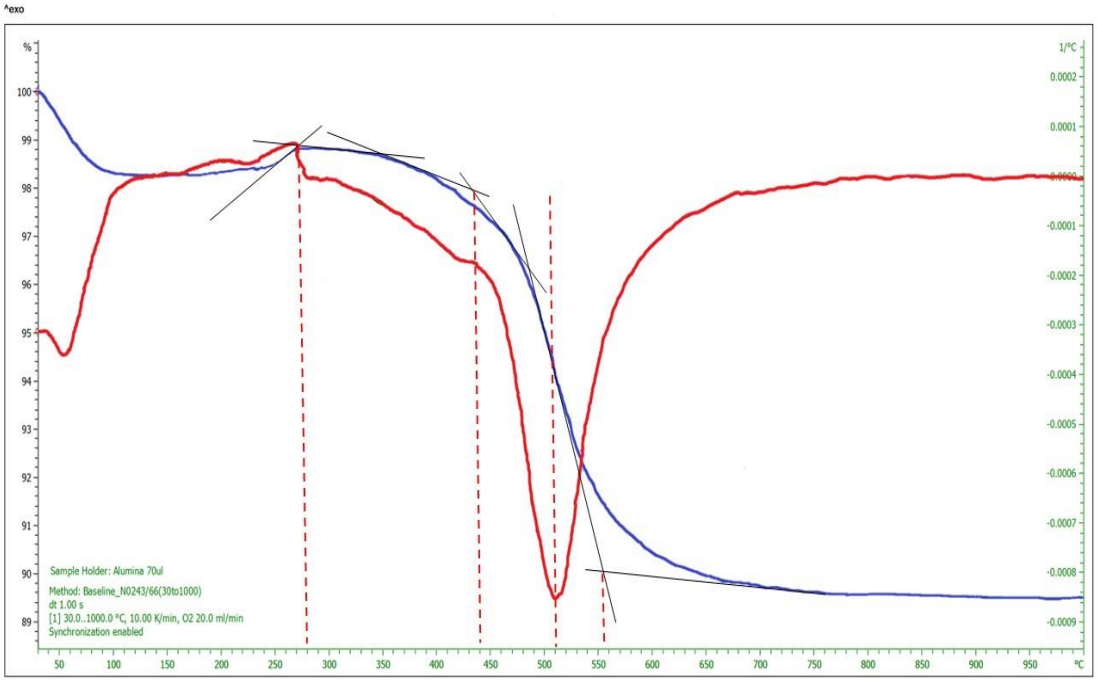

Figure 4.1 TGA and DTA curves of ball clay.

4.3 X-Ray Diffraction (XRD) Analysis

Figure 4.2 illustrates the X-ray diffraction (XRD) patterns of the raw clay materials. The major crystalline phases identified in Lampang white clay, Ranong white clay, and ball clay are kaolinite, illite, and quartz, which are considered impurity phases. In addition, ball clay was selected as the raw material for subsequent hydrothermal synthesis based on its chemical composition determined by X-ray fluorescence (XRF) analysis. The Si/Al ratio of ball clay was found to be 1.32, which is close to the theoretical Si/Al ratio of zeolite A. This appropriate compositional ratio makes ball clay a suitable precursor for the successful synthesis of Na-A zeolite under hydrothermal conditions. After calcination at 600 °C, the XRD pattern of ball clay metakaolin shows the disappearance of the characteristic kaolinite peaks when compared with that of the raw ball clay. This indicates that the kaolinite phase was

destroyed during thermal treatment as a result of dihydroxylation of the structural hydroxyl groups within the clay minerals. Consequently, the crystal structure of ball clay was transformed into an amorphous phase. This transformation is consistent with the Differential Thermal Analysis (DTA) results presented in Figure 4.1, which reveal a significant endothermic reaction associated with the loss of structural water due to dehydroxylation at the calcination temperature. Furthermore, calcination plays a crucial role in the synthesis of Na-A zeolite from ball clay, as it disrupts the original lattice structure and converts the clay into a highly reactive amorphous (metastable) phase. XRD analysis confirms that ball clay undergoes complete amorphization at approximately 600 °C, as evidenced by the absence of kaolinite reflections, with only the diffraction peaks corresponding to quartz remaining, as shown in Figure 4.3.

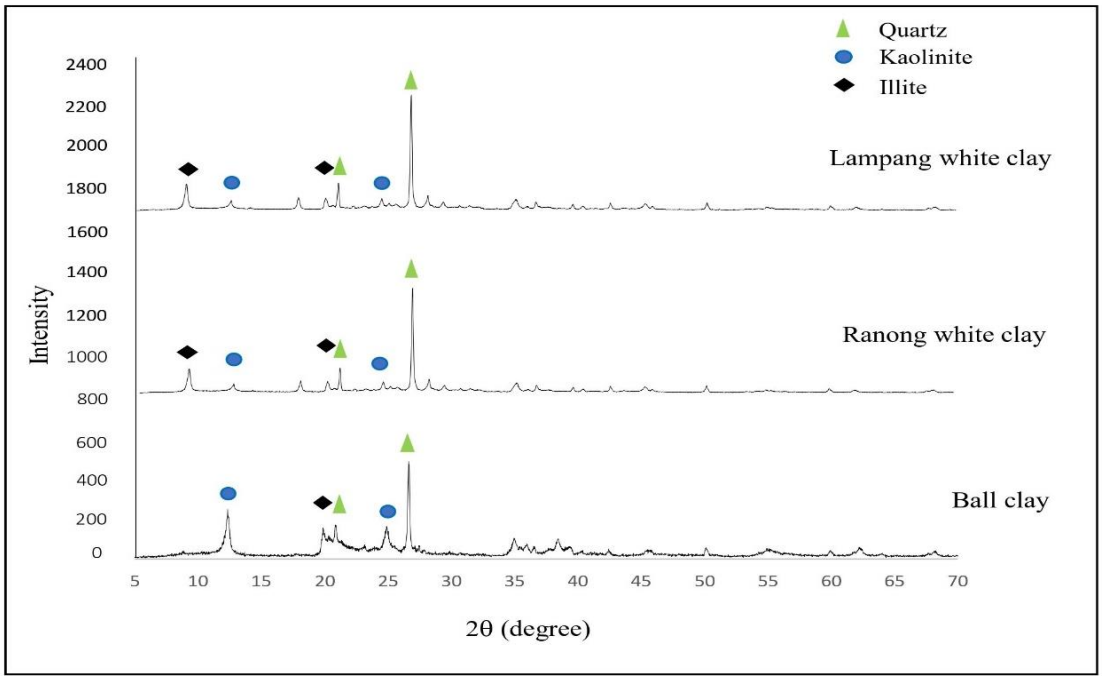

Figure 4.2 XRD pattern of clay in Thailand

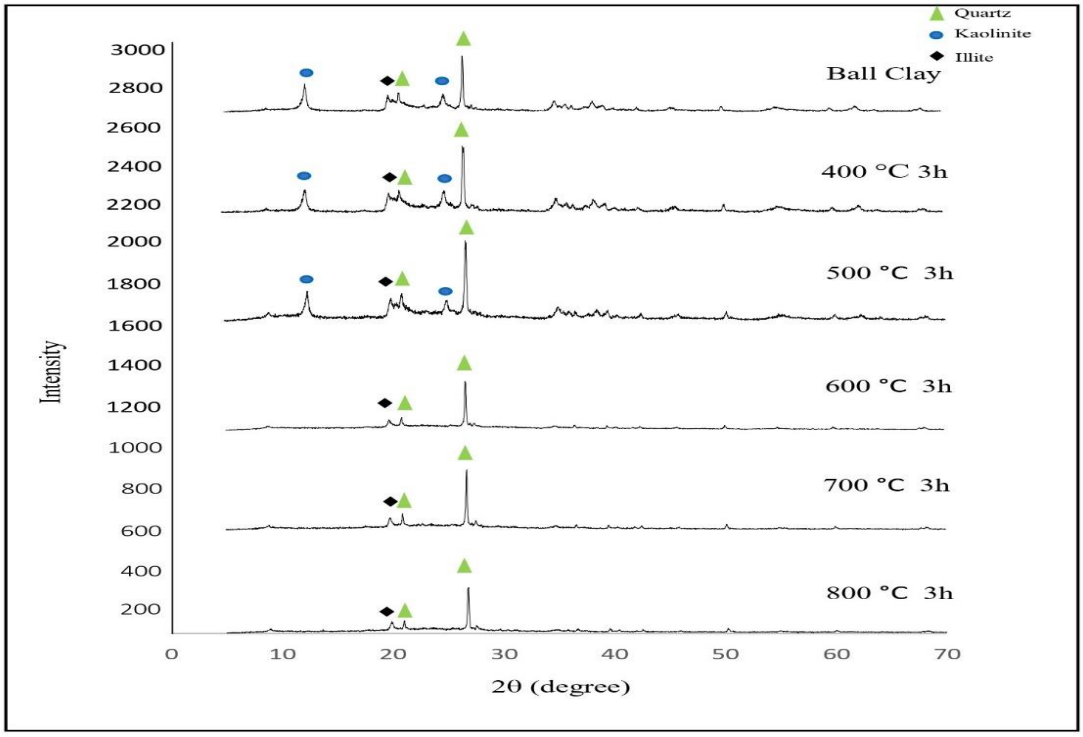

Figure 4.3 XRD pattern of ball clay and metastable phase samples calcined at a temperature range of 400 – 800 ℃ for 3 h.

Metakaolin obtained from the calcination of ball clay at 600 ℃ was used as the aluminosilicate precursor for the synthesis of Na-A zeolite via the hydrothermal method. Various factors influence the synthesis of Na-A zeolite. This study observed that the factors affecting the synthesis of Na-A zeolite were the concentrations of sodium hydroxide solution. Figure 4.4 demonstrates the XRD patterns of Na-A zeolite synthesized using different concentrations of NaOH solution. At 0.5 and 1 M NaOH, no zeolite crystal phase was observed, demonstrating that these conditions did not yield Na-A zeolite. The optimum conditions for synthesizing Na-A zeolite were achieved using NaOH concentrations of 2 and 3 M, a hydrothermal treatment temperature of 100 ℃, and a reaction time of 24 hours, which agrees with the corresponding patterns available in the literature (Silva et al., 2021). Among these conditions, the Na-A zeolite

synthesized using 3 M NaOH exhibited the highest crystallinity, as evidenced by the sharp and intense characteristic diffraction peaks of the LTA-type structure. Therefore, this sample was selected as the precursor material for the subsequent synthesis of Li-A zeolite via the cation exchange process. The ion exchange was carried out using LiOH solutions with different concentrations to investigate the effect of lithium content on the structural characteristics of the resulting Li-A zeolite. Moreover, Figure 4.5 demonstrates the XRD patterns of Li-A zeolite after cation exchange. Moreover, Figure 4.5 demonstrates the XRD patterns of Li-A zeolite after cation exchange. The reduced cation radius of Li in comparison to Na results in a structural contraction, along with minor alterations in peak intensity ratios and shifts when Na cations are substituted by other alkali metals (Price et al., 2017). X-ray diffraction (XRD) patterns of Na-A zeolite 3M and after ion exchange with lithium ions, Li-A zeolite. The diffraction peaks of both samples correspond well to the characteristic reflections of the LTA-type zeolite structure, indicating that the framework structure was preserved after the ion exchange process. A slight shift of the diffraction peaks toward higher 2 theta values was observed for the Li-A zeolite compared to the Na-A zeolite sample. For example, the characteristic reflection shifted from approximately 7.18° in Na-A zeolite to 7.25° in Li-A zeolite, while similar trends were observed for other major reflections, such as (220), approximately 10.20° in Na-A zeolite to 10.14° in Li-A zeolite, and (222), approximately 12.50° in Na-A zeolite to 12.70° in Li-A zeolite. This peak shift can be attributed to a decrease in the interplanar spacing (d-spacing), which is associated with lattice contraction caused by the replacement of Na^+ ions with smaller Li^+ ions. The ionic radius of Li^+ (0.76 Å) is smaller than that of Na^+ (1.02 Å), resulting in stronger electrostatic interactions between Li^+ ions and the negatively charged AlO_4^- units in the zeolite framework. Consequently, the unit cell parameter of the Li-A zeolite slightly decreased. Despite the observed peak shift, no additional diffraction peaks corresponding to impurity phases were detected, confirming that the ion exchange process did not alter the crystalline phase of the zeolite A structure.

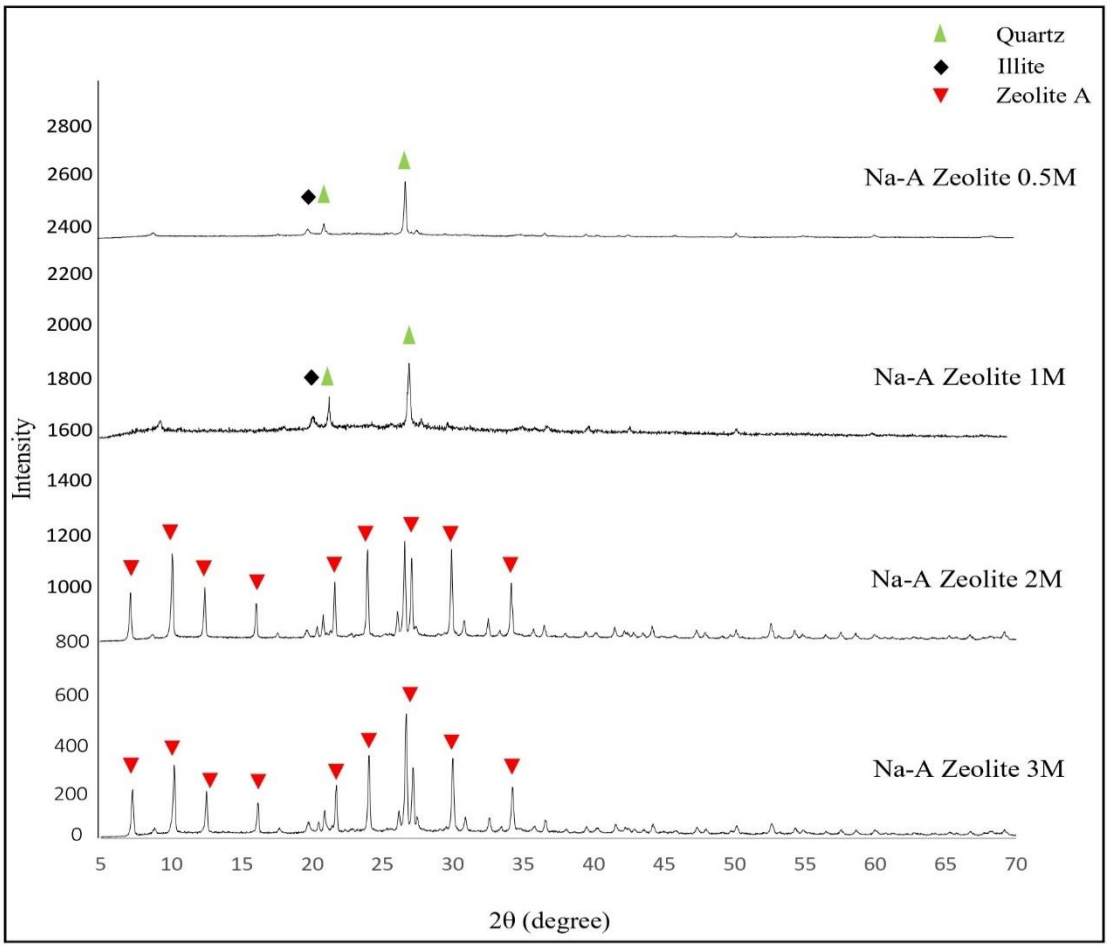

Figure 4.4 The XRD patterns of Na-A zeolite prepared by hydrothermal treatment at 100 °C in the NaOH solution at different concentrations (0.5, 1, 2, and 3 M).

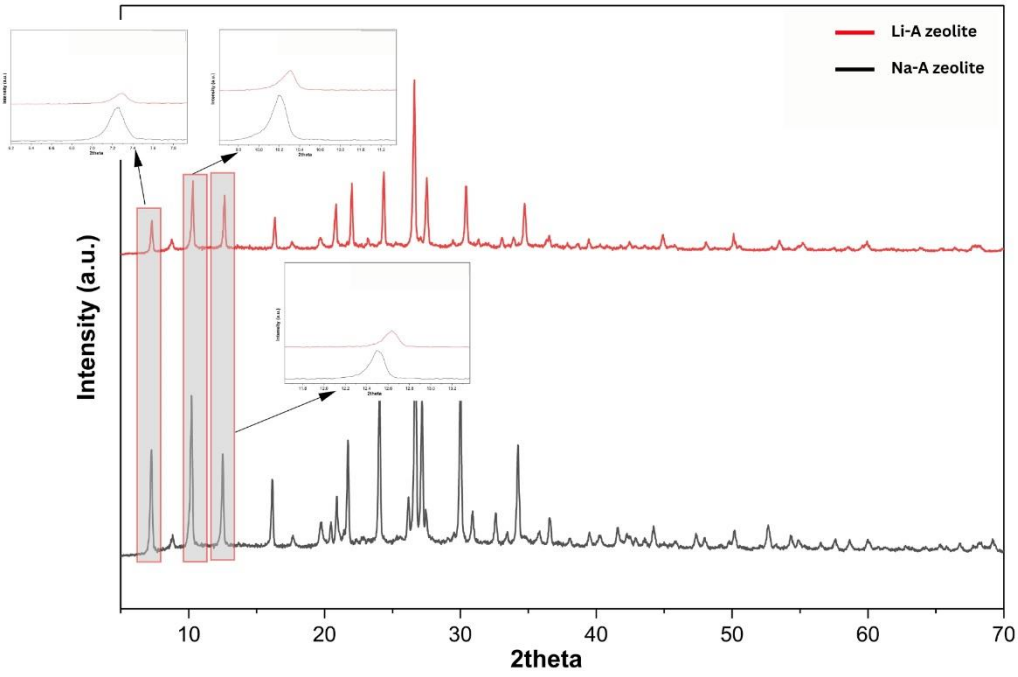

Figure 4.5 The XRD patterns of Na-A zeolite prepared by hydrothermal treatment at 100 °C in the NaOH solution 3M, and Li-A zeolite prepared by an ion-exchanger at room temperature in the LiOH solution 2M.

4.4 Fourier Transform Infrared (FTIR) Spectrum Analysis

The FTIR spectra for Na-A and Li-A zeolite display the fundamental V_{max} framework vibrations at 977 and 964 cm^{-1}, consistent to the asymmetric $V_{(O\text{-}T\text{-}O)}$ stretch. Moreover, the symmetric $V_{(O\text{-}T\text{-}O)}$ stretch occurs at 655 and 683 cm^{-1} for Na-A and Li-A zeolite, respectively. The band located at 1635 cm^{-1} is corresponded to the interstitial bonded water, and the band located between 2900 – 3750 cm^{-1} results from intra-and intermolecular hydrogen bonding (Cui et al., 2018). The FTIR results correspond with the XRD data, the framework $V_{(O\text{-}T\text{-}O)}$ asymmetric stretch shifts to a slightly lower wavenumber with increasing cation size, $Li^+ < Na^+$, as shown in Figure 4.6

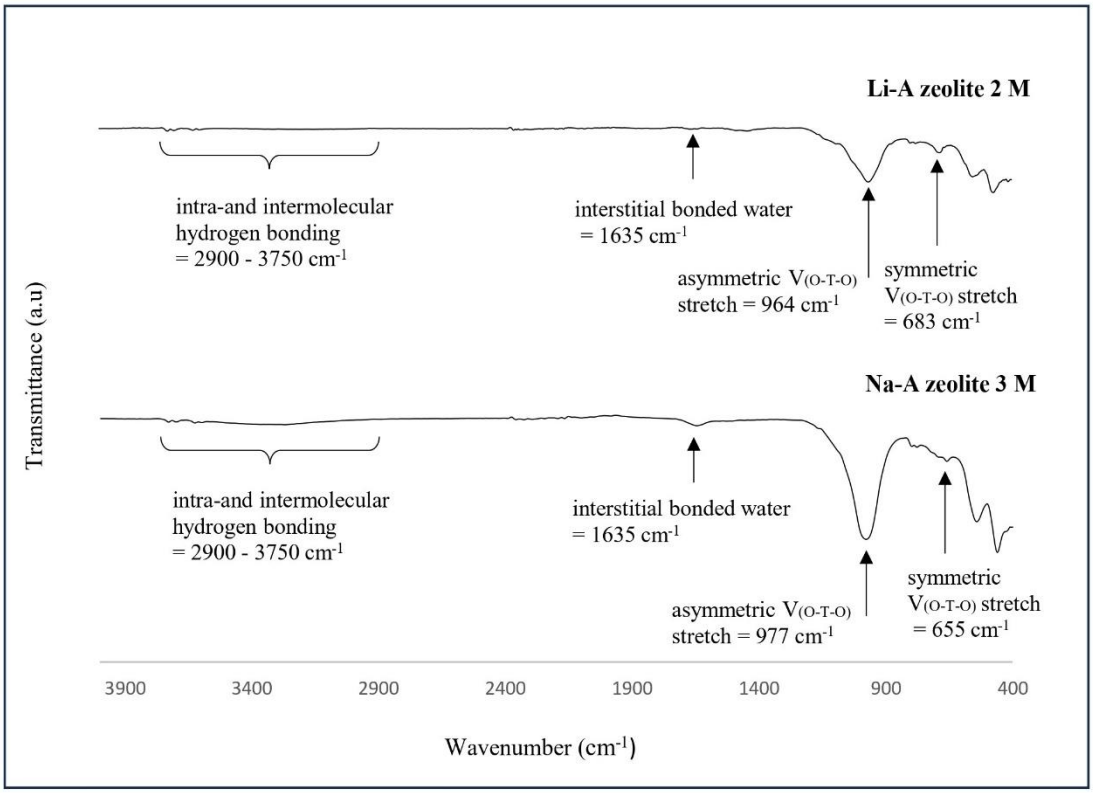

Figure 4.6 Fourier transform infrared (FTIR) spectrum of

Na-A zeolite 3M and Li-A zeolite 2M.

4.5 Scanning Electron Microscope (SEM), Energy Dispersive X-Ray Spectroscopy (EDS) Analyses, and X-Ray Tomographic Microscopy (XTM)

The micrographs in Figure 4.7a, 4.7b, and 4.7c show that the crystallites of ball clay, Lampang white clay, and Ranong white clay are in a random orientation before treatment. In contrast, the morphology of the Na-A zeolite samples after hydrothermal treatment in NaOH solutions of varying concentrations was analyzed using scanning electron microscopy (SEM). Figure 4.8 (a-d) presents the effect of NaOH concentration on the formation of Na-A zeolite obtained after activation of metakaolin at 100 °C for 24 h. The results demonstrated that the morphologies of Na-A zeolites were similar to those reported in studies on the XRD patterns of Na-A zeolite prepared by hydrothermal treatment at 100 °C in NaOH solution concentrations of 0.5, 1, 2, and 3 M. A well-defined cubic-shaped morphology of Na-A zeolite was observed at high concentrations of NaOH (2 and 3 M), as shown in Figures 4.8c and 4.8d. At NaOH concentrations of 0.5 and 1 M, the formation of Na-A zeolite was not observed, as evidenced by the absence of cubic morphology, as depicted in Figures 4.8a and 4.8b. Of all NaOH concentrations investigated, 3 M NaOH was the most suitable concentration for obtaining Na-A zeolite with a cubic morphology.

Figure 4.9a illustrates the morphology of Li-A zeolite after cationic exchange. The results demonstrated the presence of a cubic-shaped morphology in Li-A zeolite. Moreover, Figure 4.9b presents the spherical shape with a smooth surface of Li-A zeolite granules prepared by a spray dryer.

The X-ray Tomographic Microscopy experiment was conducted at beamline 1.2 at the Synchrotron Light Research Institute, Nakhon Ratchasima, Thailand. There is a distribution of particle sizes, shapes, and morphologies of ball clay (Figure 4.10a, 4.10c), and some of the ball clay particles contain inter-voids to appear hollow. The equivalent spherical diameter distribution (Figures 4.10b and 4.10d) shows particles with an average equivalent spherical diameter of 450 μm. At this magnification, the differences in greyscale are directly proportional to the atomic number of the

component that absorbs the X-ray. Moreover, the individual components of the Li-A zeolite inside each particle were resolved.

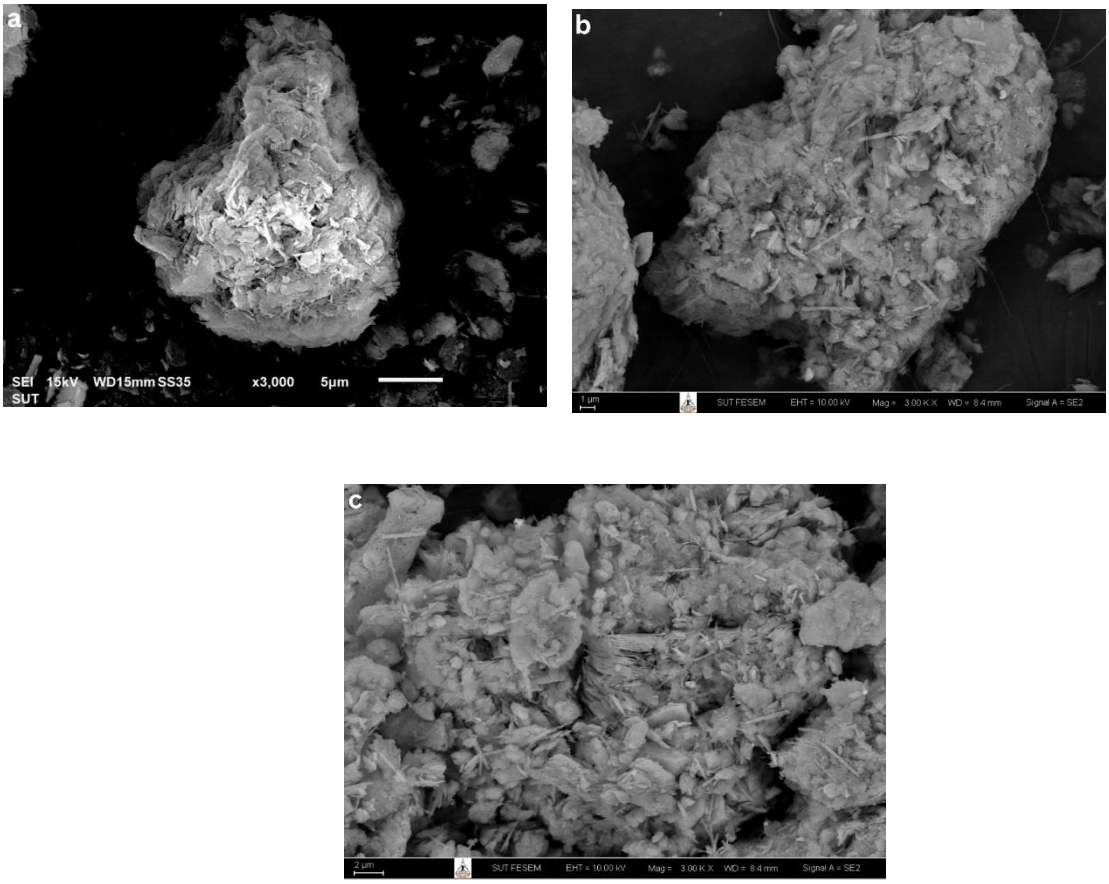

Figure 4.7 Scanning electron microscope (SEM) images of clay in Thailand

(a) Ball clay, (b) Lampang white clay, and (c) Ranong white clay

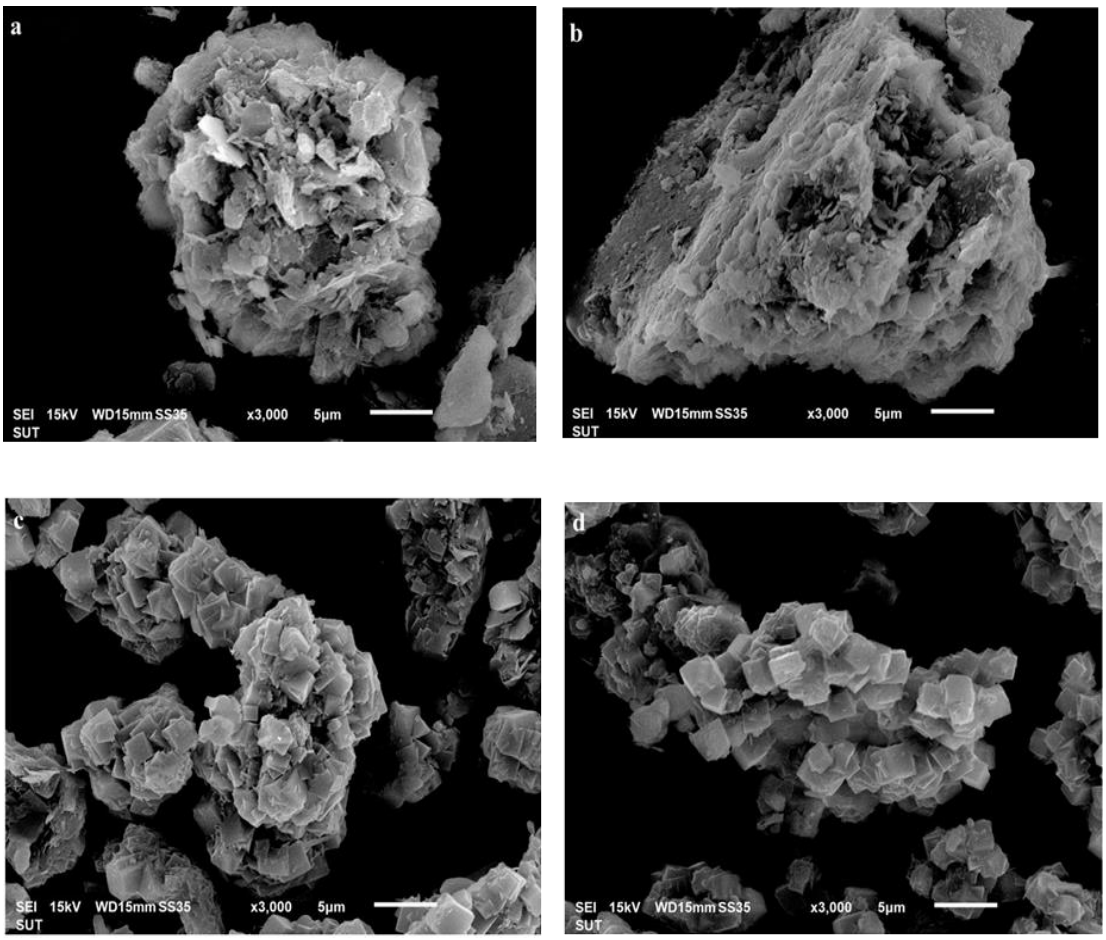

Figure 4.8 Scanning electron microscope (SEM) images of Na-A zeolite after hydrothermal treatment in NaOH solution at various concentrations: (a) 0.5 M, (b) 1 M, (c) 2 M, and (d) 3 M

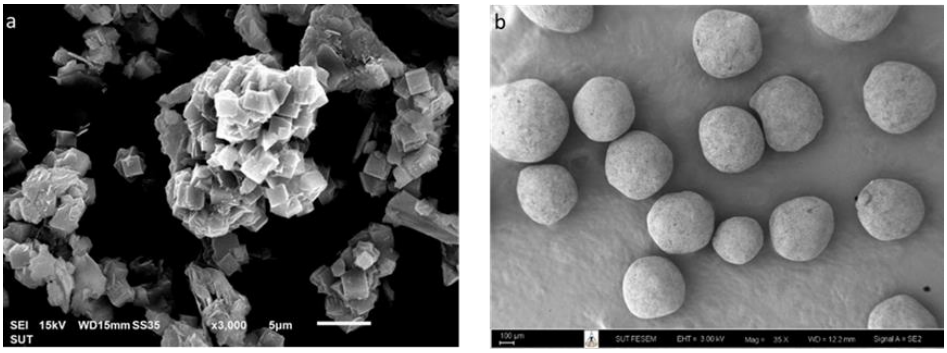

Figure 4.9 Scanning electron microscope (SEM) images of (a)Li-A zeolite after a cationic exchange in LiOH solution at 2M and (b)Li-A zeolite granules prepared by a spray dryer

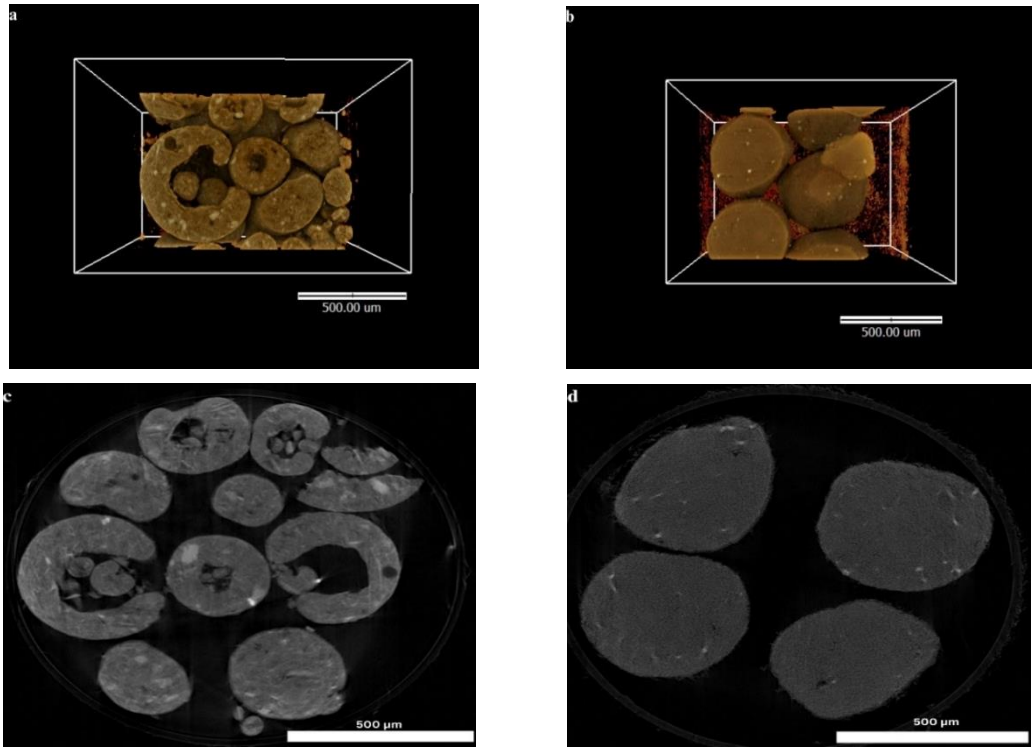

Figure 4.10 Cross-section of the 3D image of (a)ball clay, (b) Li-A zeolite granules and a single slice of the tomogram of (c) ball clay and (d) Li-A zeolite granules

4.6 Specific Surface Area of Li-A Zeolite

The textural properties of the synthesized Li-A zeolite were analyzed by Brunauer–Emmett–Teller (BET) surface area analysis using nitrogen adsorption–desorption measurements at 77 K. The synthesized Li-A zeolite exhibited a specific surface area of 450 m^2/g, depending on synthesis temperature, NaOH, and LiOH concentration. These values are slightly lower than those of commercial zeolite A (Typically 500-800 m^2/g). This relatively high surface area indicates the successful development of a well-defined microporous framework characteristic of zeolite A. The total pore volume of the synthesized Li-A zeolite is 0.25 cm^3/g, which is comparable to previously reported values in the range of 0.20–0.35 cm^3/g for conventional zeolite A materials. The pore volume is mainly attributed to the intrinsic microporous structure of zeolite A, consisting of sodalite cages interconnected by uniform pore openings. The average pore size of the synthesized Li-A zeolite is 0.4 nm, confirming that the material predominantly exhibits microporosity. This value is consistent with reported average pore sizes for zeolite A, which are generally below 2 nm, corresponding to the characteristic pore opening of approximately 0.4 nm. Such pore dimensions are favorable for molecular sieving and selective adsorption applications. Overall, the specific surface area, total pore volume, and average pore size of the synthesized zeolite A are in good agreement with values reported in previous studies, indicating that the synthesized material possesses typical textural properties of zeolite A and is suitable for adsorption and molecular sieving applications.

4.7 Zeolite molecular sieve for oxygen concentrator

This chapter presents the experimental results of the zeolite samples with particle sizes of 450 μm, 550 μm, and 650 μm, tested in the oxygen concentrator system. The main objective was to evaluate the relationship between particle size and oxygen purity (%).

4.7.1 Oxygen Purity of Different Zeolite Particle Sizes

The results demonstrated a clear relationship between zeolite particle size and oxygen purity produced by the oxygen concentrator. The performance evaluation was conducted over three independent test cycles, with each cycle operated continuously for 2 h to ensure reproducibility and operational stability. The obtained results showed consistent trends across all test runs. As the zeolite particle size decreased, the oxygen purity increased. Specifically, the zeolite with a particle size of 450 μm exhibited the highest performance, achieving a maximum oxygen purity of 93%. In comparison, the 550 μm zeolite sample reached a maximum oxygen purity of 92%, while the 650 μm sample showed the lowest performance, with a maximum oxygen purity of 90%. These results indicate a gradual decrease in oxygen separation efficiency with increasing particle size. The improved performance observed for smaller particle sizes can be attributed to the increased surface area, which promotes more effective nitrogen adsorption during the pressure swing adsorption (PSA) process. Importantly, oxygen purity levels exceeding 90% are generally considered acceptable and suitable for typical medical oxygen concentrator applications. Therefore, all tested zeolite particle sizes met the minimum requirement for medical use; however, the 450 μm zeolite demonstrated superior performance and is the most suitable particle size among the samples investigated.

Table 4.2 Oxygen purity at different zeolite particle sizes

Time (min)	O_2 Purity (%)								
	450 µm			550 µm			650 µm		
	1st	2nd	3rd	1st	2nd	3rd	1st	2nd	3rd
5	92	92	92	91	92	91	90	90	88
10	92	92	92	92	92	92	88	90	90
15	93	93	93	92	92	92	88	89	88
20	91	92	91	91	91	91	89	89	89
25	92	91	92	90	90	92	89	90	90
30	92	92	92	90	90	90	90	90	90
35	93	93	93	91	90	91	89	89	89
40	91	92	91	91	91	91	90	88	90
45	91	91	91	91	91	91	90	89	89
50	91	91	91	91	91	91	90	90	90
55	91	91	91	91	91	91	88	88	88
60	90	92	93	90	90	90	90	90	90
65	90	90	93	92	92	92	89	89	89
70	90	91	92	90	90	90	90	90	90
75	91	91	91	91	91	91	88	88	88
80	91	91	93	91	91	91	88	89	89
85	90	92	92	90	90	90	90	90	90

Table 4.2 Oxygen purity at different zeolite particle sizes (Continued)

Time (min)	O_2 Purity (%)								
	450 µm			550 µm			650 µm		
	1st	2nd	3rd	1st	2nd	3rd	1st	2nd	3rd
90	91	93	91	91	92	91	88	88	90
95	91	91	91	91	92	91	89	88	89
100	91	91	91	91	91	91	89	89	89
105	91	91	91	91	91	91	89	90	90
110	93	93	93	92	92	92	90	90	90
115	93	93	93	91	91	91	90	88	90
120	92	92	92	90	92	90	90	90	89

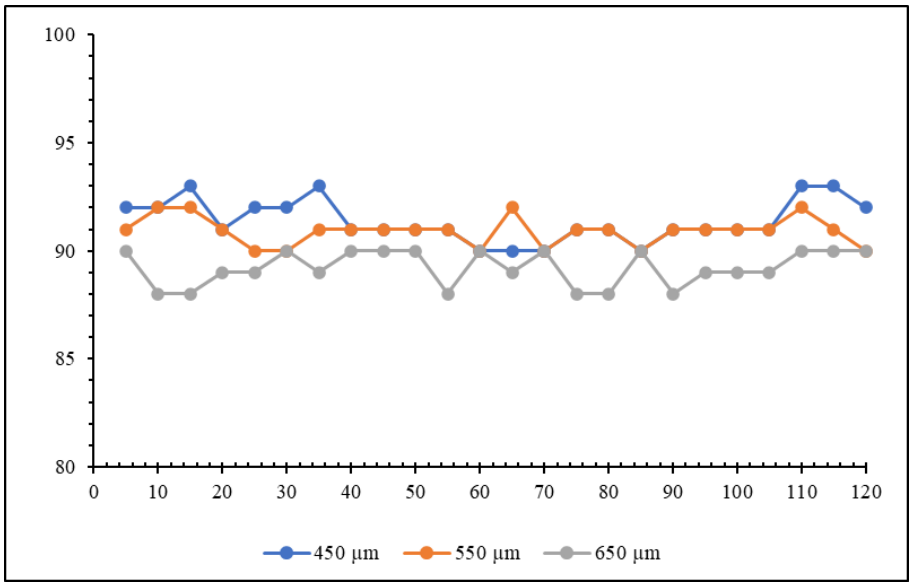

Figure 4.11 The first cycle of the oxygen concentrator at different zeolite particle sizes

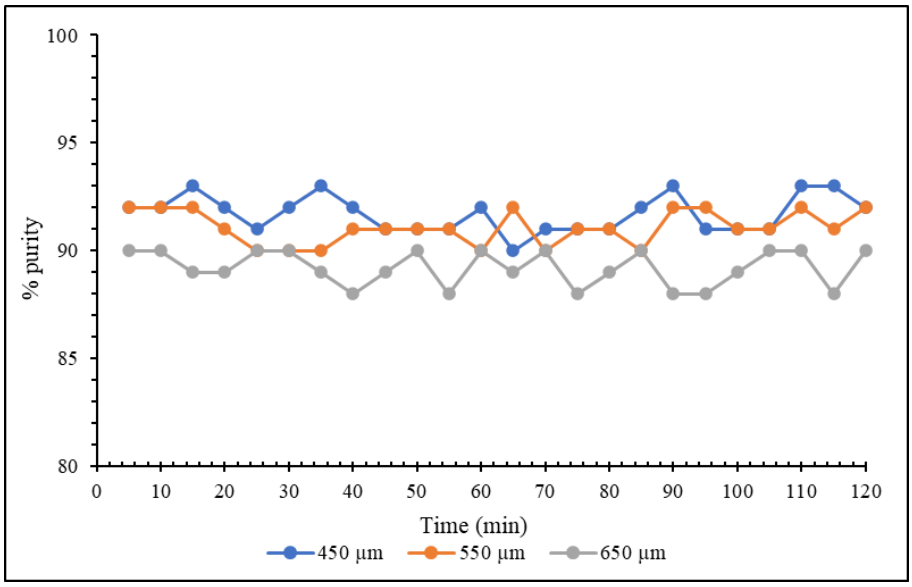

Figure 4.12 The second cycle of the oxygen concentrator at different zeolite particle sizes

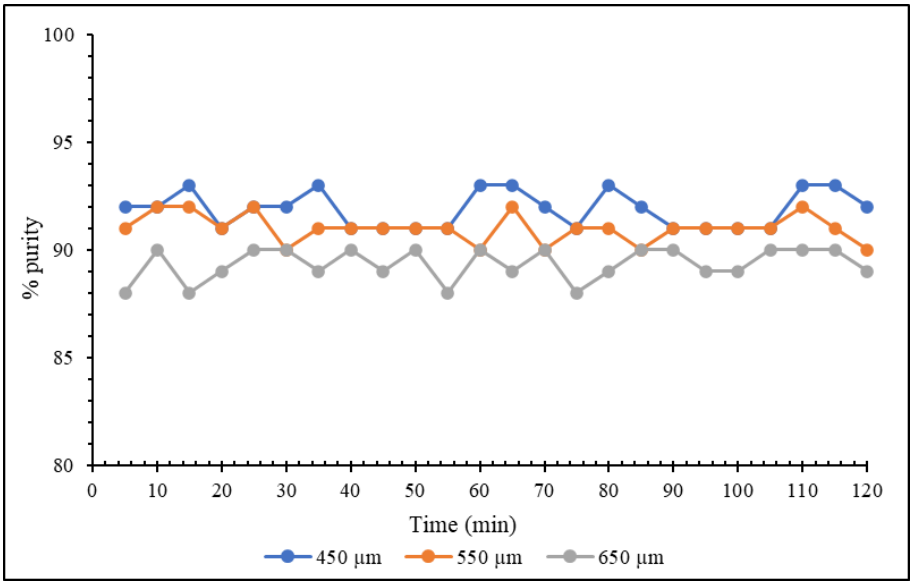

Figure 4.13 The third cycle of the oxygen concentrator at different zeolite particle sizes